

Article

Wave–Tide Interaction by Typhoon Ampil on Wave and Storm Surge in the Changjiang River Estuary and Its Adjacent Coastal Areas

Yuting Zhang, Qiyang Ji *, Minghong Xie, You Wu and Yilun Tian

Marine Science and Technology College, Zhejiang Ocean University, Zhoushan 316022, China; zhangyuting@zjou.edu.cn (Y.Z.); xieminghong@zjou.edu.cn (M.X.); wuyou@zjou.edu.cn (Y.W.); tianyilun@zjou.edu.cn (Y.T.)

* Correspondence: jiqiyang@zjou.edu.cn; Tel.: +86-0580-2661857

Abstract: The study used the SCHISM ocean model combined with the WWM III wind wave model to quantify the interaction between wind waves and tides in the coastal zone of the Changjiang River Estuary and its adjacent areas. The wave and storm surge during Typhoon Ampil, which made landfall in July 2018 in Shanghai, were simulated by using the Climate Forecast System Version 2 (CFSv2) and Medium-Range Weather Forecasts (ECMWF) latest reanalysis (ERA5) wind dataset from 1 July to 31 July. Model results with CFSv2 forcing show better performance in terms of significant wave height and storm surge than those with ERA5 forcing. To investigate the interactions between waves, water levels, currents, and their combined effects on significant wave and surge variations, six numerical sensitivity experiments were designed according to the different coupling methods between SCHISM and WWMIII. The research shows that in coastal areas with water depths of less than 10 m, waves are affected by water levels and currents. The differences in the effect on significant wave height between wave-tide coupling and one-way coupling with water levels and currents are negligible. Wave setup is an important physical term which cannot be ignored during the variations of storm surge caused by Typhoon Ampil. The contributions of wave set up were concentrated in coastal areas with water depths less than 10 m. The peak wave setup occurred in the Changjiang River Estuary, reaching 0.15 m. In Xiangshan Bay and Sanmen Bay, wave radiation stress makes the proportion of wave setup to the total surge reached more than 30%. The consideration of wave-tide interaction can effectively improve the accuracy of numerical wave and storm surge simulations, which can provide more accurate hindcasts of wave and storm surge variations in the Changjiang River Estuary and its adjacent coastal areas.

Keywords: wave-tide interaction; typhoon; significant wave height; wave setup; storm surge



Citation: Zhang, Y.; Ji, Q.; Xie, M.; Wu, Y.; Tian, Y. Wave–Tide Interaction by Typhoon Ampil on Wave and Storm Surge in the Changjiang River Estuary and Its Adjacent Coastal Areas. *J. Mar. Sci. Eng.* **2023**, *11*, 1984. <https://doi.org/10.3390/jmse11101984>

Academic Editor: Kamal Djidjeli

Received: 9 August 2023

Revised: 28 September 2023

Accepted: 11 October 2023

Published: 13 October 2023



Copyright: © 2023 by the authors. Licensee MDPI, Basel, Switzerland. This article is an open access article distributed under the terms and conditions of the Creative Commons Attribution (CC BY) license (<https://creativecommons.org/licenses/by/4.0/>).

1. Introduction

The Changjiang River Estuary and its adjacent coastal areas, located on the east coast of China and the northwestern Pacific Ocean, are the areas where usually hit by typhoons. They are surrounded by the Shanghai, Zhejiang and Jiangsu provinces, which are the most economically developed regions in China. The total number of typhoons affecting the Changjiang River Estuary area from 1949 to 2018 is 160, with an average of 2.3 per year [1]. These areas are vulnerable to typhoon-induced massive ocean waves and storm surges. The combined waves and surges cause flooding in regions susceptible to typhoon, especially when they occur coincidentally at high tides [2,3]. Over the past 30 years, many typhoons have struck this coastal area, causing severe coastal flooding, infrastructure damage and huge economic losses [4]. For example, the super typhoon Chan-hom in 2015 caused economic losses of over RMB 9.8 billion [5]. However, due to the complex coastline and topography, as well as the many offshore islands, it is complex and difficult to accurately predict the storm surge and waves in the Changjiang River Estuary and adjacent seas.

Before the 21st century, the study and prediction of storm surges and waves have been carried out separately due to theoretical and technical limitations. The statistical methods were usually used for the study and prediction of storm surge [6–9] and ocean waves [10,11]. However, these methods are usually based on observation data and are limited by special conditions. Currently, the most widely used method for storm surge and wave are the numerical models, which based on physical dynamics. The ocean models based on the Navier-Stokes equation are used for numerical simulation and prediction of storm surge and inundation (e.g., ADCIRC [12], FVCOM [13], Delft3D [14], Mike21 [15], ROMS [16]). The results of numerical simulations of storm surges are influenced by open boundary conditions [17,18], spatial resolution [19,20] and pattern regions [21,22]. In addition to these purely numerical model settings, in practice storm surge is also influenced by typhoon intensity, maximum wind speed radius, moving speed, landfall direction and topography [23–28]. In the numerical prediction of typhoon waves, most of the third-generation wave models such as SWAN [29] or WAVEWATCH III [30] are used, and many studies have been conducted to improve wave prediction accuracy on the basis of the bottom friction scheme and nonlinear coupling between waves [31,32]. In addition to numerical modelling, machine learning methods are increasingly being used to predict the storm surges and waves. However, these methods also require large amounts of data for training to get reasonable prediction results [33–38].

Numerous studies have shown non-linear coupling between tides, waves and currents [39–42]. The wave will modify the storm surge as it propagates and generate wave-generated currents in the nearshore [43,44], while storm surges can also have a deforming effect on waves [45–47]. In order to accurately simulate and predict the real process of storm surge and ocean waves, it is necessary to consider the coupling effect of waves-tides-currents in the numerical model. The concept of wave radiation stress provides the theoretical basis for the construction of a coupling wave-tide model, which explains the phenomena of wave-induced storm surges and wave-induced currents [48,49]. There are many coupling tide-wave models such as POM + SWAN [50], ADCIRC + SWAN [51,52], ROMS + SWAN [53,54], FVCOM + SWAVE [55,56], which are widely used to predict storm surges and waves. These coupling models are also used to study the interactions between waves and tides and currents. Xie et al. study wave effects on storm surge and flooding in Charleston Harbors under the influence of Hurricane Hugo using a coupling POM + SWAN model [50]. Using the coupling SCHISM-WWMII model, Laura Lavaud found that wave radiation stress contributed 23–40 percent of the water levels rise in the Bay of Biscay during Tropical Storm Klaus [57]. Christo Rautenbach quantifies the proportion of wave-induced surge and storm surge in complex orographically shaped inlets in the South African region using online coupling of Delft3D and SWAN, where the proportion of wave-induced water gain is around 20% [58]. Soo Youl Kim et al. studied the effects of tides on surges, wave setups and waves in terms of tidal amplitudes and phases using a coupling numerical model of surge, wave and tide (called SuWAT). The results show that surge and wave setups increase during low tide phases and decrease during high tide phases [59]. Baptiste Mengual studied the interactions between waves and currents in the Tagus estuary using the coupling SCHISM-WWM III model and found that the tidal currents can change not only the height of the waves but also their direction [60].

There are also many studies on storm surges and waves and their interaction in the marginal seas of China based on the coupling wave-tide numerical model. Du et al. used the coupling ADCIRC + SWAN model to analyze the impacts of 55 historical tracks from 1951 to 2017 on the coast of Zhejiang Province, China [61]. He et al. study the interaction effects of tides and waves in the port of Yangshan in China during Typhoon Chan-Hom using the coupling model FVCOM + SWAVE. The results show that the contribution of wind to the peak storm surge was 87.1%, followed by pressure-induced surge (23.7%) and wave-induced surge (14.4%) during Typhoon Chan-Hom [62]. Hsiao et al. quantified the contribution of nonlinear interactions to storm surge simulations around Taiwan during Super Typhoon Meranti in 2016, concluding that storm surge miscalculations can be avoided

by including wave motion when predicting typhoon-induced storm surges [63]. Song et al. studied wave-current interactions in the Bohai Sea using the coupling Delft3D + SWAN model. They found that wave-current interactions increase the friction on the seafloor, which reduces the velocity of the current by 15 percent [64].

However, research on quantifying the contribution of nonlinear interactions to storm surge and wave simulations in the Changjiang River Estuary and its adjacent seas areas. Understanding the interactions between waves and storm surges, as well as the effects of tides on significant wave height, is beneficial for improving the accuracy of storm surge and wave predictions. The influence of the tides in these areas is significant, dominated by semi-diurnal tides with a tidal range of 3 to 6 m. This study focuses on the interactions between waves and tides in the Changjiang River Estuary and its adjacent sea areas during Typhoon Ampil, which made landfall in Shanghai on 22 July 2018. The typhoon data is collected from the Tokyo-Typhoon Center of the Japan Meteorological Agency (JMA). The track of Typhoon Ampil in 2018 and the bathymetric is shown in Figure 1. To address these critical research questions, a series of numerical experiments have been conducted to performed using the different coupling methods of SCHISM and WWMIII.

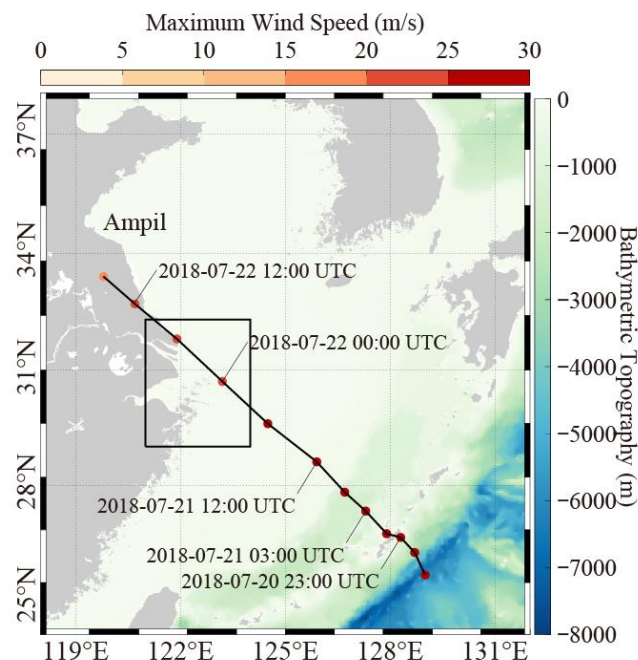


Figure 1. The track of Typhoon Ampil in 2018 and the bathymetric for SCHISM-WWMIII.

Structurally, the paper quantified the wave-surge interactions during Typhoon Ampil through the designed experiments. The rest of this paper is organized as follows. Section 2 presents the model, the model configuration and the observational data. In Section 3, the simulation results of the model are examined. The results and discussion of the wave-tidal interaction are presented in Section 4. Conclusions are given in Section 5.

2. Methods and Datasets

2.1. Numerical Model

2.1.1. SCHISM Hydrodynamic Model

The Semi-implicit Cross-scale Hydroscience Integrated System Model (SCHISM) is used to study storm surge and waves in the Changjiang River Estuary and adjacent coastal sea. SCHISM is a seamless cross-scale model based on unstructured grids, derived from SELFE, which can be coupled with various models and has been widely used in the studies of oceans and estuaries in different locations [65,66].

The governing equations of SCHISM are the Navier-Stokes equations, which are solved using fluid statics and the Boussinesq approximation. The governing equations are as follows:

$$\frac{D\vec{u}}{dt} = \vec{f} - g\nabla\eta + \vec{m}_z - \alpha|\vec{u}|\vec{u}L(x, y, z) \tag{1}$$

$$\nabla \cdot \vec{u} + \frac{\partial w}{\partial z} = 0 \tag{2}$$

$$\frac{\partial \eta}{\partial t} + \nabla \cdot \int_{-h}^{\eta} \vec{u} dz = 0 \tag{3}$$

$$\frac{\partial C}{\partial t} + \nabla \cdot (\vec{u}C) = \frac{\partial}{\partial z} \left(\kappa \frac{\partial C}{\partial z} \right) + F_h \tag{4}$$

$$\rho = \rho(S, T, p) \tag{5}$$

Equation (1) is the momentum equation. It is solved by the Eulerian-Lagrangian method. \vec{f} represents the external forces received during the motion process, including the baroclinic gradient, horizontal viscosity, Coriolis force, Earth tidal potential, atmospheric pressure, and radiation stress. $\vec{f} = f(v, -u) - \frac{g}{\rho_0} \int_z^{\eta} \nabla \rho d\xi - \frac{\nabla p_A}{\rho_0} + \alpha g \nabla \Psi + \vec{F}_m + other$. Equations (2) and (3) are continuity equations, which ensure the conservation of mass within the system. Equation (4) is the transport equation, which can be solved for tracers simultaneously to improve computational efficiency. Equation (5) is the equation of state, which relate the density of the fluid to its temperature, salinity, and pressure. In the governing equations, g represents the acceleration of gravity, η is the free-surface elevation, u is the horizontal velocity, α is the effective earth-elasticity factor, p is the atmospheric pressure at mean sea level, ρ is the density of water, \vec{F}_m is the horizontal viscosity, C is the tracer concentration which represents variables such as salinity, temperature, sediment, etc. κ is the vertical eddy diffusivity for tracers, F_h is horizontal diffusion and mass sources/sinks. In the two-dimensional model, \vec{m}_z represents the vertical eddy viscosity.

2.1.2. WWMIII Wave Model

The Wind Wave Model-III (WWM-III) model [67,68] utilizes an unstructured grid, optimized and developed based on the code of Hsu et al. [69]. The model is improved in terms of both computational performance and physical mechanisms. The numerical computation scheme employs a sparse matrix solver, which makes a significant improvement in computational speed compared to previous versions. The dissipation term function is modified to a saturation-based dissipation function, which improves the simulation results. The wave action equation is expressed as follows:

$$\frac{\partial}{\partial t} N + \nabla_X (\dot{X}N) + \frac{\partial}{\partial \sigma} (\dot{\theta}N) + \frac{\partial}{\partial \theta} (\dot{\sigma}N) = S_{tot} \tag{6}$$

$$N_{(t,X,\sigma,\theta)} = \frac{E_{(t,X,\sigma,\theta)}}{\sigma} \tag{7}$$

$$\dot{X} = c_X = \frac{dX}{dt} = \frac{d\omega}{dk} = c_g + U_A \tag{8}$$

$$\dot{\theta} = c_\theta = \frac{1}{k} \frac{\partial \sigma}{\partial d} \frac{\partial d}{\partial m} + \vec{k} \cdot \frac{\partial U_A}{\partial s} \tag{9}$$

$$\dot{\sigma} = c_\sigma = s \frac{\partial \sigma}{\partial d} \left(\frac{\partial d}{\partial t} + U_A \cdot \nabla_X d \right) - c_g k \frac{\partial U_A}{\partial s} \tag{10}$$

There are four terms in Equation (6), representing the temporal variation of the wave action, the refraction caused by currents and depth, and the frequency shift due to depth variation and currents, respectively. In the equation, N represents the wave action density spectrum, E represents the variance density associated with a particular spectral segment ($d\sigma, d\theta$). The coordinates s and m represent the direction of wave propagation and the direction perpendicular to it, respectively. In the absence of currents, the advection velocity in the σ direction is zero, and in deep water with no currents, the θ component is zero. S_{tot} is the source function, which includes wind energy input, nonlinear interactions in deep and shallow water, energy dissipation due to whitecapping and wave breaking in deep and shallow water, wave dissipation caused by bottom friction, and nonlinear interactions between waves and the seabed.

The wave radiation stress is solved based on the formula proposed by Longuet-Higgins and Stewart [48], which is transferred to the hydrodynamic model in the coupling process. The calculated currents and water levels are then fed back into Equations (8)–(10). The wave action equation is then solved. Then, the coupling between the two models is achieved.

2.2. Model Configurations

The SCHISM and WWMIII model use the same unstructured grid for parallel computations, as shown in Figure 2. The model domain covers the East China Sea and parts of the Northwest Pacific (18.74–43.21° N, 117.55–143.28° E), including three open boundaries. The grid is encrypted the offshore ports and waterways of Changjiang River Estuary and adjacent seas, with a total of 117,402 grid points and 225,323 triangular elements. The horizontal spatial resolution of the model ranges from about 0.16 km to 16 km. Vertically, the Sigma coordinate system is used, with a uniform division into nine layers. Coastline data are derived from the GSHHG (Global Self-consistent, Hierarchical, High-resolution Geography Database) dataset [70]. Topographic data are obtained from the GEBCO (General Bathymetric Chart of the Oceans), with a 1/240° horizontal resolution [71], while for the southeastern coastal area the ENCs (Electronic Navigational Charts) is used.

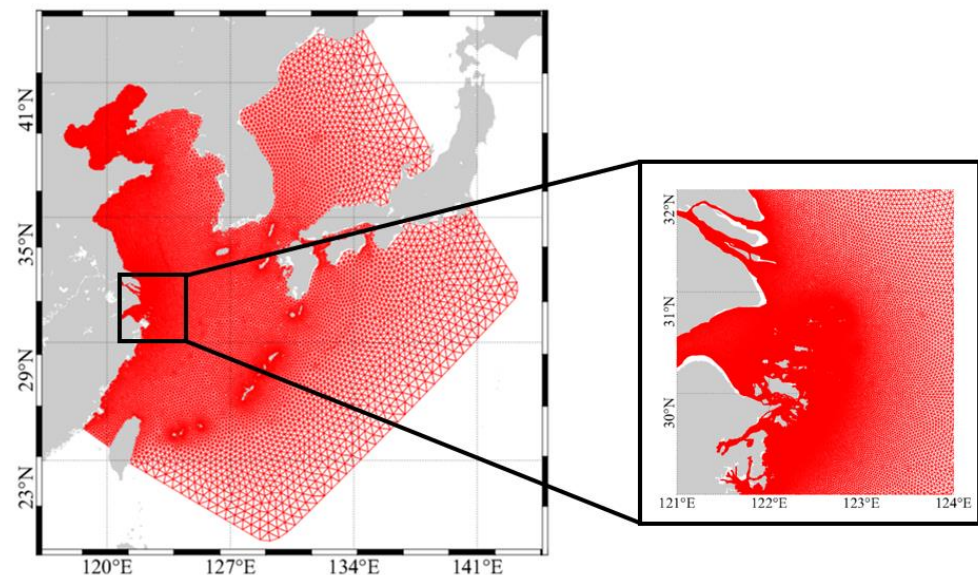


Figure 2. Computational mesh for the SCHISM-WWMIII.

The global ocean tide model FES2014 [72] with a horizontal resolution of 1/16° is used to specify the tidal forcing at the open boundaries of SCHISM. The 10 main tidal components, including 8 main components are as follows: M2, S2, K1, O1, N2, K2, P1, Q1. In addition, 2 long-period constituents (Mf and Mm) were extracted from the FES2014 global tidal model.

Wind fields are important for the effect of significant wave height and storm surge. In this paper, the wind fields and sea level pressure (SLP) fields from the NCEP Climate Forecast System Version 2 (CFSv2) [73] and the European Centre for Medium-Range Weather Forecast (ECMWF) fifth generation reanalysis (ERA5) [74] were used as the atmospheric forcing for SCHISM. The WWMIII model used the same atmospheric forcing data as the SCHISM. The information of the wind fields is shown in Table 1.

Table 1. Information of wind dataset.

Dataset Name	Time	Spatial Resolution	Temporal Resolution
CFSv2	1 July 2018–31 July 2018	0.205° × 0.204°	1 h
ERA5	1 July 2018–31 July 2018	0.25° × 0.25°	1 h

The Battjes and Janssen [75] and Joint North Sea Wave Project (JONSWAP) [76] schemes were used for the shallow water wave breaking formulation and the wave dissipation by bottom friction, respectively. The wave breaking coefficient, bottom friction coefficient and peak enhancement were set to 0.78, 0.067, and 3.3, respectively, which are the default setting values of the wave model. The wave frequencies were discretized into 36 bins ranging from 0.03 Hz to 1.0 Hz, and the wave directions were discretized into 36 bins ranging from 0° to 360°. The time step for SCHISM is set to 120 s. The time step for the WWMIII model is set to 600 s, and the model outputs results every hour. A one-month simulation from 1 July 2018 to 31 July 2018 was conducted by the SCHISM-WWMIII.

2.3. Numerical Experiments

The coupled SCHISM-WWMIII is used to simulate storm surges and waves during Typhoon Ampil (2018). The effects of wave-tide interaction (WTI) in the Changjiang River Estuary and adjacent seas are estimated using the results of 6 experiments conducted with the SCHISM-WWMIII (Table 2).

Table 2. Simulation settings for each experiment.

Simulation	Forcing in SCHISM	Forcing in WWMIII
Exp1	Tide, wind, SLP, wave	elevation, current, wind
Exp2	Tide, wind, SLP	elevation, current, wind
Exp3	Tide, wind, SLP,	current, wind
Exp4	Tide, wind, SLP,	elevation, wind
Exp5	\	Wind
Exp6	Tide	\

In each experiment, a different way of running the coupling model is used: tide-surge-wave, tide-surge, wave-only, and tide-only. One fully coupling model run (Exp1) is performed for validation. The experiment2, experiment3, experiment4 (Exp2, Exp3, Exp4) were run in the way of tide-surge. To investigate the dominant factors for significant wave height (SWH) modulation, the effects of currents (Exp3), water levels (Exp4) are respectively applied to the one-way coupling model run. A wave-only model run (Exp5) is driven by wind to simulate wind-induced waves. A tide-only model run (Exp6) is driven by astronomical tides. More detailed descriptions of the model runs are given in Table 1.

In this study, we focused on the wave-tide interactions during Typhoon Ampil. The key issue is how to quantify the nonlinear term. The quantified physical terms can be obtained through the above experiments. Storm surge is typically calculated by subtracting the astronomical tide from the total water levels [45,59]. By analyzing the results of experiments Exp1 and Exp6, it is possible to calculate the storm surge height:

$$\eta_s = \eta_{wec} - \eta_t, \tag{11}$$

where η_s represents the storm surge water levels, which is the combination of the total water levels simulated by the Exp1 experiment (η_{wec}) and the astronomical tide level simulated by the Exp6 experiment (η_t).

To calculate the influence of tidal effects on the significant wave height from a physical oceanographic perspective, the significant wave height simulated in the fully coupling experiment (Exp1) can be compared with the significant wave height driven by wind forcing alone (Exp5). The wave heights in both experiments can be expressed as follows:

$$H_t = H_{wec} - H_{ow}, \tag{12}$$

where H_{wec} is the wave height simulated in the Exp1 experiment, which takes into account the coupling between waves, water levels and currents. H_{ow} is the wave height simulated in the Exp5, where only the wind forcing is considered.

To compare the fully coupling experiment (Exp1) with the one-way coupling experiment (Exp2) where water levels and currents are used as driving conditions for wave height, the wave height H in both experiments can be expressed as follows:

$$H_{wti} = H_{wec} - H_{ec}, \tag{13}$$

where H_{ec} is the SWH simulated in the Exp2, using water levels and currents as the driving conditions.

Wave setup is the increase of water levels caused by the breaking of waves as they approach the shore. It is the result of the wave radiation stress which can contribute to higher water levels during storm surge events. Both the Exp1 and Exp2 experiments are driven by wind and tides, but in the Exp2 experiment, the hydrodynamic model neglects the wave radiation stress. Therefore, the wave setup can be quantified by comparing the results of Exp1 and Exp2 as:

$$\eta_w = \eta_{wec} - \eta_{ec}, \tag{14}$$

where η_{wec} represents the total water levels simulated by Exp1, η_{ec} represents the total water levels simulated by the Exp2, and η_w refers to the water levels change caused by wave radiation stress.

2.4. Observed Data

Typhoon Ampil was generated in the Pacific Ocean at 20:00 p.m. on 18 July 2018, made landfall on Chongming Island in Shanghai, around 12:30 on 22 July 2018. The Table 3 shows the track of Typhoon Ampil. The wind vector maps of the typhoon landfall process are shown in Figure 3. During the landfall, there was an astronomical low tide, and the tidal range near the Changjiang River estuary was around 2.0 m.

The simulated SWH and water levels data were validated to assess the accuracy of the model. The observed SWH data from the “2010–2018 Typhoon Dataset in the Yellow Sea and East China Sea” published by the Chinese Academy of Sciences [77]. The dataset includes data from 21 sets of buoys located in the Yellow Sea and East China Sea, which collected meteorological, hydrological, and water quality data. SWH time series were obtained from buoys No.06, No.10, No.11, No.12, No.14, and No.20 in the East China Sea during the passage of Typhoon Ampil. Buoy 06 recorded observations with a sampling interval of 30 min, while the remaining buoys recorded observations every 10 min. The recording periods varied slightly for each buoy, but all included the growth and decay of waves as the typhoon passed. The locations of buoys are shown in Figure 4.

Table 3. Information of Typhoon Ampil from JMA.

Time	Lat (°)	Lon (°)	Pre (hPa)	Wind (kt)
20 July 2018 09:00	23.8	130.3	985	50
20 July 2018 12:00	24.5	129.9	985	50
20 July 2018 15:00	24.9	129.5	985	50

Table 3. Cont.

Time	Lat (°)	Lon (°)	Pre (hPa)	Wind (kt)
20 July 2018 18:00	25.6	129.0	985	50
20 July 2018 21:00	26.2	128.7	985	50
20 July 2018 23:00	26.6	128.3	985	50
21 July 2018 00:00	26.7	127.9	985	50
21 July 2018 03:00	27.3	127.3	985	50
21 July 2018 06:00	27.8	126.7	985	50
21 July 2018 12:00	28.6	125.9	985	50
21 July 2018 18:00	29.6	124.5	985	50
22 July 2018 00:00	30.7	123.2	985	45
22 July 2018 06:00	31.8	121.9	985	45
22 July 2018 12:00	32.7	120.7	985	40
22 July 2018 18:00	33.4	119.8	990	35
22 July 2018 00:00	34.5	119.2	992	35
22 July 2018 06:00	35.1	118.7	992	35

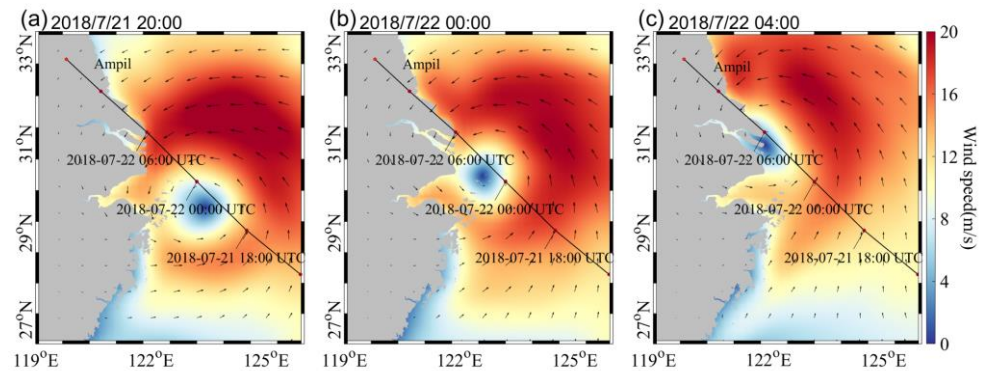


Figure 3. Wind vector maps during the passage of Typhoon Ampil are shown for (a) 21 July, 20:00, (b) 22 July, 0:00, and (c) 22 July, 4:00 UTC.

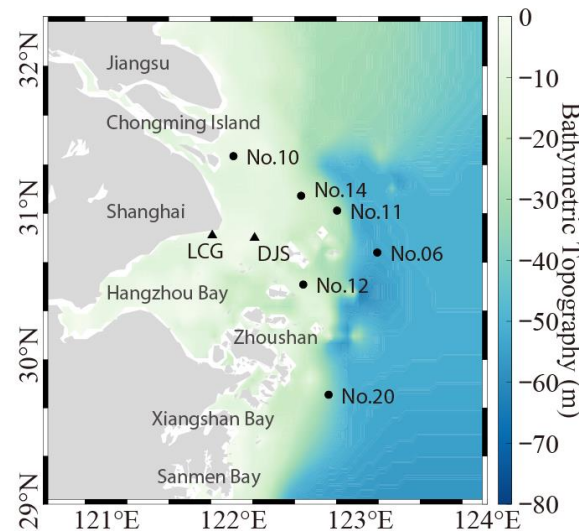


Figure 4. Bathymetric topography of Changjiang River Estuary and its adjacent coastal sea, the locations of buoys and tidal gauges indicated by dots and triangles, respectively.

Astronomical tide validation data were obtained from the National Marine Data and Information Service tide tables due to a lack of observed water levels data. Storm surge data were obtained from two tidal gauge stations: Luchaogang (LCG) and Dajishan (DJS). These tidal gauge stations recorded hourly observations from 21 July, 00:00 to 24 July, 23:00. The locations of the buoys and tidal gauge stations are shown in Table 4.

Table 4. Model validation locations of buoys and tide gauges.

Measurement	Name	Latitude	Longitude
Wave buoy	No.06	30°43' N	123°08' E
	No.10	31°22' N	122°00' E
	No.11	31°00' N	122°49' E
	No.12	30°30' N	122°33' E
	No.14	31°06' N	122°32' E
	No.20	29°45' N	122°45' E
Tidal gauge	Luchaogang	30°50' N	121°50' E
	Dajishan	30°49' N	122°10' E

3. Model Assessments

3.1. Validation of Wave

Figure 5 shows the time series of the simulated and observed SWH at the wave buoys by applying different wind fields during the typhoon passage. The CFSv2 wind field vector is shown in Figure 3. The maximum wave heights are 9 m (No.06 and No.11), 8 m (No.14 and No.20), 7 m (No.12) between 1:00 a.m. and 6:00 a.m. on 22 July, when the typhoon was approaching Zhoushan offshore area. The maximum SWH is less than 2 m at buoy No.10, which is located near Chongming Island, where the water depth is shallow. In addition, the SWH time series of buoy No.10 also shows a periodic variation compared to other buoys. The main reason for this phenomenon will be discussed in Section 4.1 of this paper.

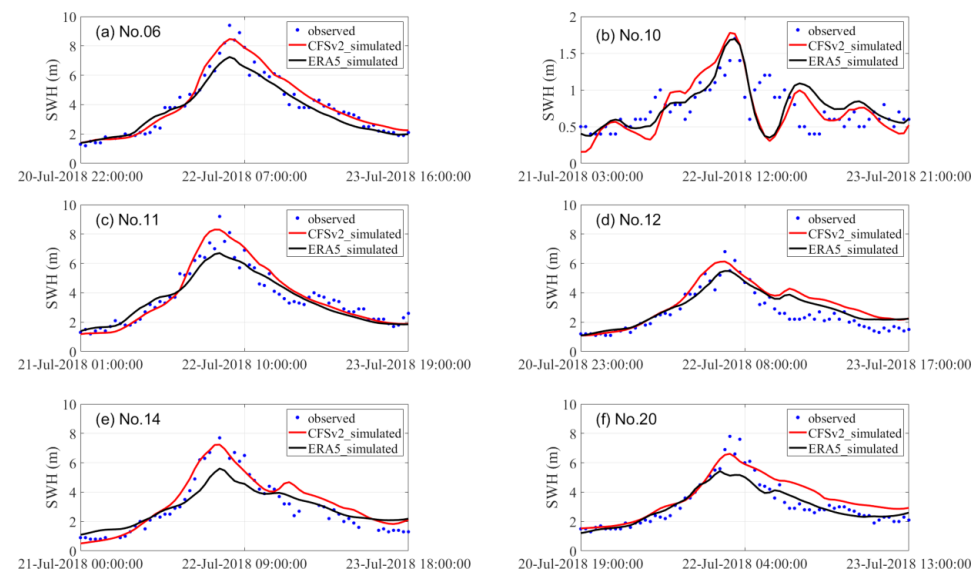


Figure 5. Time series of observed and simulated significant wave heights from 21 July to 23 July at (a) buoy No.6, (b) buoy No.10, (c) buoy No.11, (d) buoy No.12, (e) buoy No.14, (f) buoy No.14, respectively.

The scatter graphs between the simulated SWH forcing by the two wind fields and the observed data of the buoys are shown in Figure 6. Combined with the SWH time series in Figure 5, during the stages of wave growth and decay, the simulated SWH forcing by the CFSv2 wind field is smaller than that forcing by the ERA5 wind field. However, the peak wave heights were significantly underpredicted by the simulation results using the ERA5 wind field. Under the ERA5 wind field, the correlation coefficient and root mean square error (RMSE) for significant wave height are 0.95 and 0.41 m, respectively. In the case of the CFSv2 wind field, the correlation coefficient and RMSE for significant wave height are 0.96 and 0.33 m, respectively. The CFSv2 wind field providing superior simulations of SWH during Typhoon Ampil, the simulated results demonstrate a well agreement with observations. The bias between the observation and model results may

be caused by the disparities of water depth, underestimation of typhoon wind speeds. Physical parametrizations schemes such as the wave breaking functions and bottom friction functions may affect the performance of wave simulation. The settings of the bottom friction coefficients and wave breaking coefficients may also contribute to improve the wave height predictions.

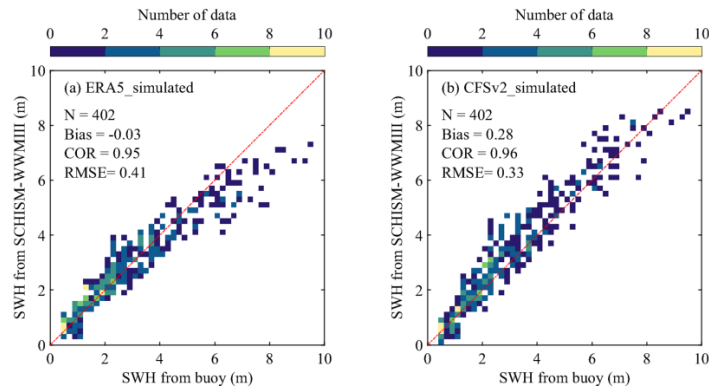


Figure 6. Comparison between simulated SWH using the ERA5 wind fields (a), the CFSv2 wind fields (b) and observed SWH from buoys.

3.2. Validation of Tide

Before conducting storm surge simulation research, it is necessary to validate the SCHISM hydrodynamic module. During tidal validation, the hydrodynamic model is configured with open boundaries driven by water levels, without considering wind fields and wave radiation stresses.

The tidal validation was carried out using tidal data from two stations, namely Luchao-gang (LCG) and Dajishan (DJS). The tidal time series are shown in Figure 7, the observed and simulated values are consistent show a generally similar trend. The correlation coefficients for tidal observations and simulations at both stations reached 0.98, with root mean square errors of 0.19 m and 0.38 m, respectively. Therefore, it can be concluded that the selection and configuration of the model can adequately capture the tidal characteristics within the study area. The sources of error may be due to the shallow water depths at the measurement sites and the omission of an optimal bottom friction scheme. In addition, there may be some errors in the initial tidal boundary conditions of the model.

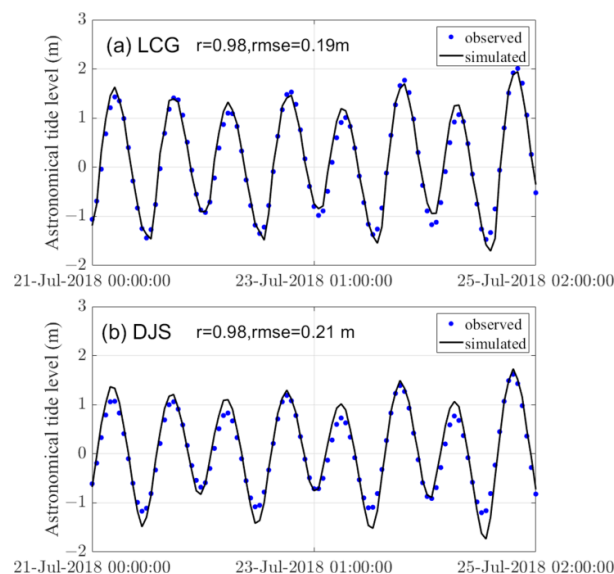


Figure 7. Time series of astronomical tide levels from tidal data and simulations at (a) LCG station and (b) DJS station.

3.3. Validation of Storm Surge

The time series of simulated and observed values for storm surge are shown in Figure 8. At the LCG station, the storm surge peaked at 0.53 m at 3:00 on 22 July. At the DJS station, the peak storm surge of 0.66 m occurred at 4:00 a.m. At this time, the wind field is shown in Figure 3a, with the measurement stations located in an area of higher wind speeds on the periphery of the typhoon. The wind speed reaches 20 m/s, blowing from the northeast, causing the seawater to accumulate towards the coast and leading to the peak water levels. According to the observed data, the surge showed an obvious downward trend at both stations. Surge didn't fall at the same time, at LCG station, the moment of surge dropping is earlier than DJS station. Considering the time of surge fall, topographic, wind field and tidal factors at LCG and DJS, the time series of storm surge can be reasonable. However, the specific process of surge at different stations is needed more experiments to research.

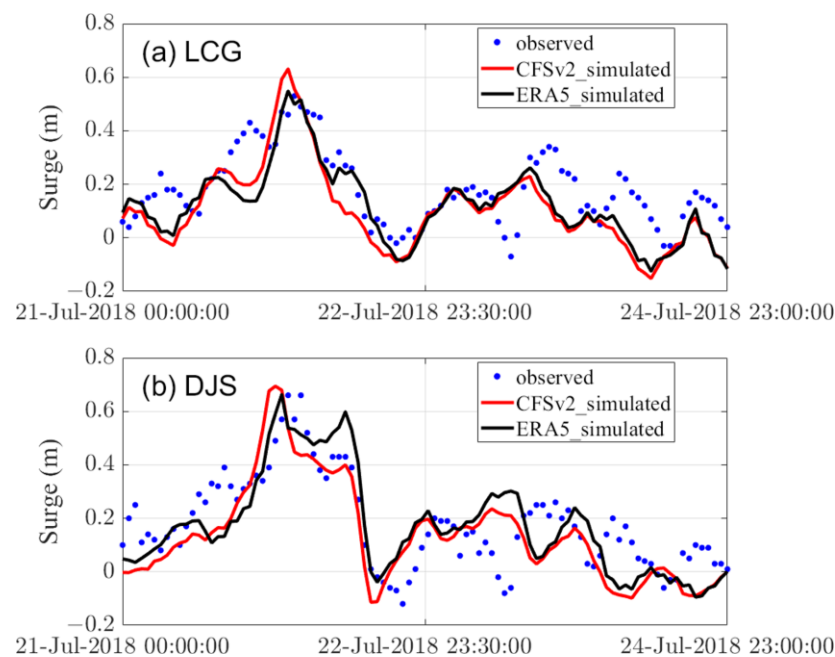


Figure 8. Time series of storm surge from observations and simulations at (a) LCG station and (b) DJS station.

Under the ERA5 wind field, storm surges at LCG station show a correlation coefficient of 0.72 with an RMSE of 0.11 m, and at DJS station, a correlation coefficient of 0.73 with an RMSE of 0.13 m. Meanwhile, under the CFSv2 wind field, LCG station exhibits a correlation coefficient of 0.74 and an RMSE of 0.12 m, while at DJS station the correlation coefficient is 0.75 with an RMSE of 0.13 m. The storm surge simulations driven by winds from the CFSv2 and ERA5 were consistent with the data from stations during Typhoon Ampil. Considering the favorable performance of the CFSv2 wind field in the simulation of significant wave heights, it is reasonable to adopt CFSv2 as the forcing wind field during Typhoon Ampil. Therefore, we focused on the study of wave-tide interactions based on the simulation results which driven by the CFSv2 in Section 4.

4. Results and Discussions

4.1. Effect of Water Levels on SWH

During the wave validation of the buoys, buoy No.10 shows a clear periodic modulation in significant wave height before and after the typhoon passage, while the other buoys did not show this phenomenon. In order to determine the factors causing wave deformation, a numerical simulation of wave propagation was carried out. The experiments (Exp1, Exp3, Exp4, Exp5) were carried out to investigate the factors causing the periodic

modulation of SWH. AB profile (from A to B) is showed on the bathymetric map, where the coordinates of point A are 121.75° E, 31.5° N, and the coordinates of point B are 123.5° E, 30.3° N. The distribution of SWH along the AB profile is shown in Figure 9. The figure depicts the time series of SWH under different conditions, including currents and wind fields (Exp3), water levels and wind fields (Exp4), wind fields (Exp5), and their combined effects (Exp1).

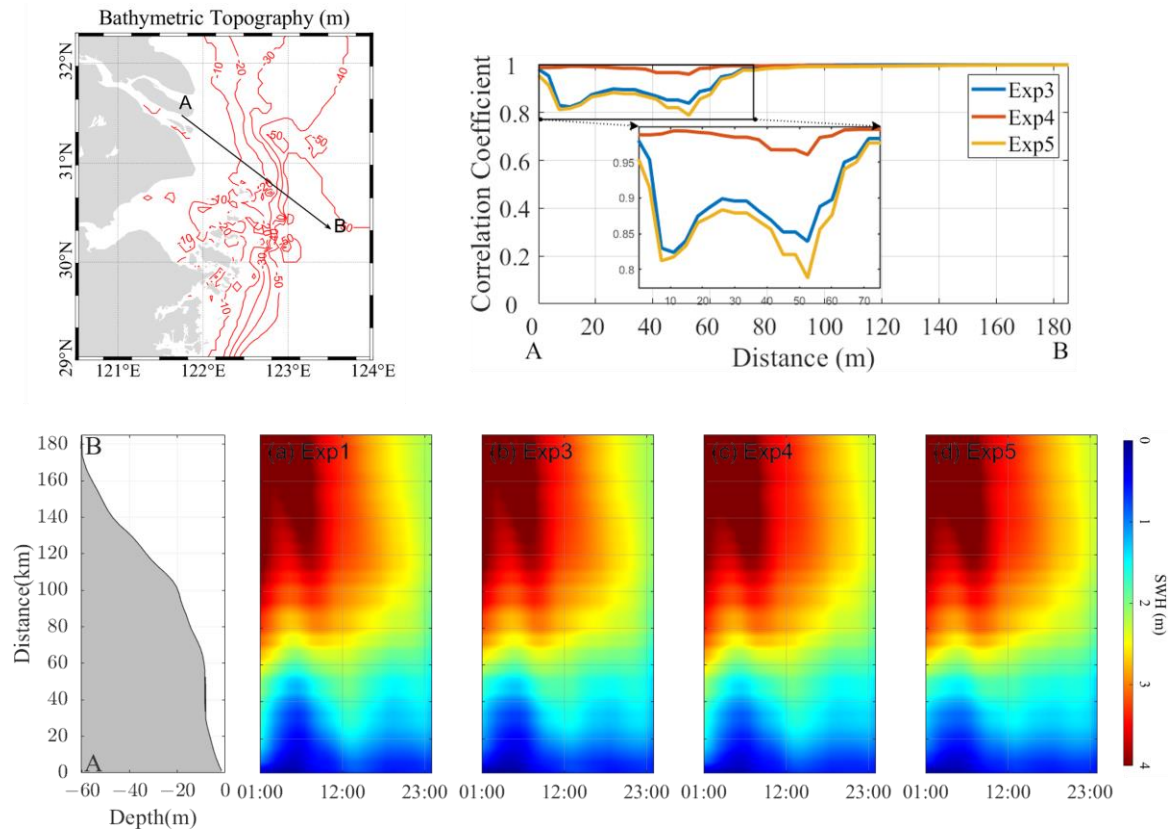


Figure 9. (Upper left) The location of AB profile. The isobaths (in meters) are red. (Upper right) The correlation coefficients of SWH between Exp3, Exp4, Exp5 with respect to Exp1. (Lower left) Bathymetric variation along the AB profile, from A (distance is 0 km) to B (distance is 185.23 km). (Lower right) Time series of SWH along the AB profile under the influence of (a) combined action (Exp1), (b) current variation and wind (Exp3), (c) water level variation and wind (Exp4), (d) wind (Exp5) The time is from 1 a.m. to 24 p.m. on 24 July.

The combined effects of currents, water levels, and wind fields on wave height are depicted in Figure 9a. To estimate the effects of currents, water levels and wind fields to the SWH modulation, their correlation coefficients are calculated and shown in Figure 9. Within a distance of about 70 km from point A and in water depths of about 10 m or less, the correlation coefficients in the three experiments (Exp3, Exp4, Exp5) have shown an obvious difference. The simulated SWH only considering wind forcing (Exp5) shows the lowest correlation of 0.78. The correlation coefficients of Exp3, which considering the effects of currents and wind forcing, is roughly consistent with Exp5. The correlation coefficients of Exp4 with a high value of more than 0.95, which shows that the SWH modulation in coastal area is mainly controlled by the water levels and wind fields. The correlation between the three experiments (Exp3, Exp4, Exp5) and the fully coupled experiment (Exp1) is almost consistent beyond 70 km from point A, where the water depth exceeds 10 m. The simulation results of Exp1, Exp3, Exp4 and Exp5 indicate that water levels changes can cause periodic modulation in wave height, especially in the shallow nearshore areas with water depths of about 10 m or less. On the other hand, when farther from the coast, in

water depths greater than 10 m, the wind field becomes the primary factor influencing the magnitude of the wave height.

4.2. Effect of Wave-Tide Interaction on SWH

The spatial distribution of the significant wave height is roughly similar in both experiments, as shown in Figure 10a,c. On 21 July at 22:00, when Typhoon Ampil approaches the vicinity of Hangzhou Bay, the maximum wave height exceeds 6 m. The difference between Exp1 and Exp5 is shown in Figure 10f, which shows that H_{wec} is smaller than H_{ow} on the right side of the typhoon track. However, on the left side of the typhoon track, especially in the Hangzhou Bay and its northern region, H_{wec} exceeds H_{ow} , with a maximum difference of 0.8 m. This result indicates that water levels and currents play a certain role in simulating the significant wave height. Furthermore, in regions with strong tides (Figure 10d), the differences in wave height are even more pronounced.

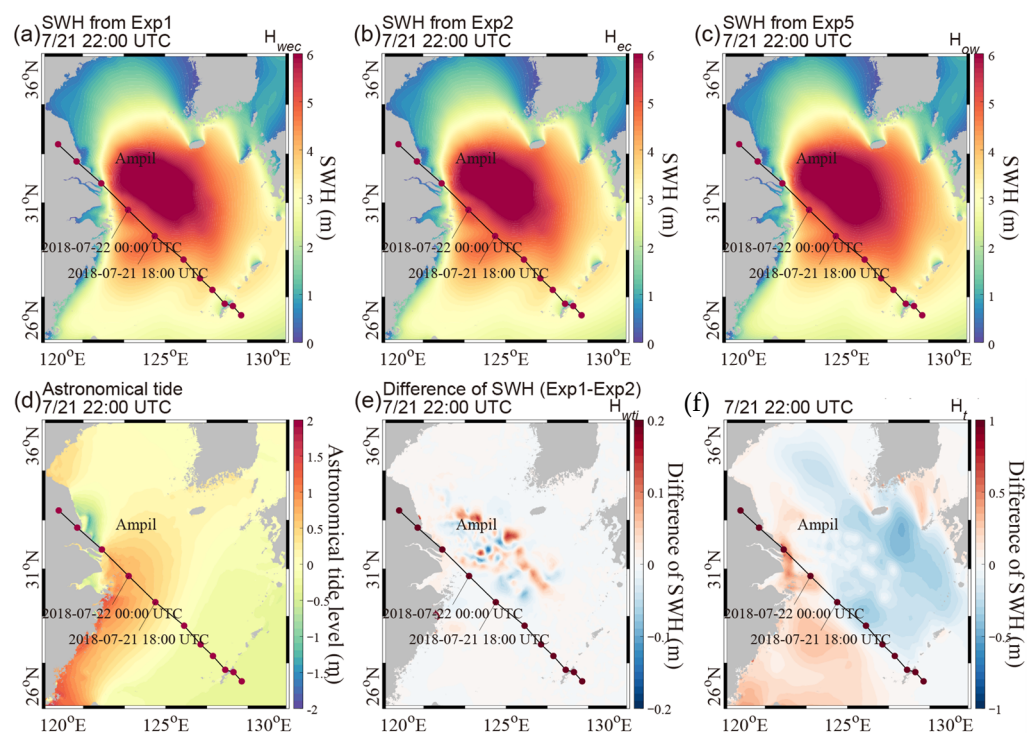


Figure 10. Spatial patterns for the SWH in Exp1 (a), Exp2 (b), Exp5 (c) and their differences (e,f) at 22:00 UTC on 21 July. Spatial patterns for tide in Exp6 (d).

The difference between Exp1 and Exp2 can be seen as the wave height variation caused by wave-tide interactions. As shown in Figure 10e, there is a difference of ± 0.2 m in wave height between Exp1 and Exp2, and this difference is mostly concentrated in the region near the center of the typhoon where the wave height is higher.

A root mean square error (RMSE) bar chart was used to compare and validate the results of Exp1, Exp2, Exp5 and the buoy measurements (Figure 11). The Exp5 shows the highest RMSE of SWH between simulated and observed. The order of magnitude from the difference in RMSE between Exp1 and Exp2 is 10^{-3} m, which shows that ways of coupling have a small impact on SWH. Both approaches perform better than wave simulations driven by wind forcing alone.

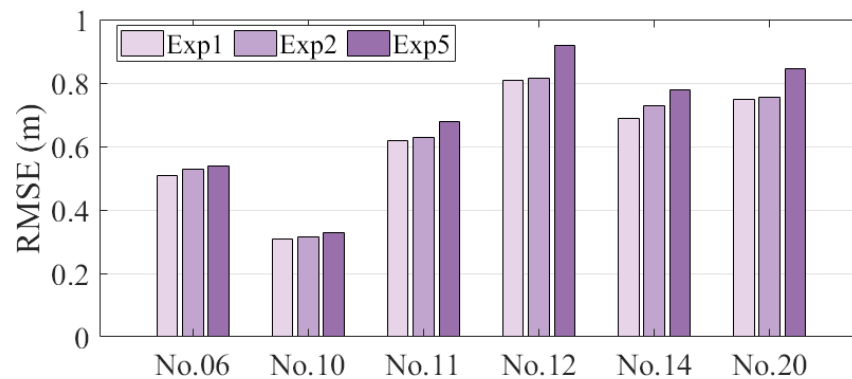


Figure 11. Bar chart of the Root Mean Square Error (RMSE) of the SWH between Exp1, Exp2, Exp5 and the buoy measurements.

4.3. Contribution of Wave Setup to Storm Surge

The time series of storm surge and wave setup for the LCG and DJS stations obtained from the Exp1 and Exp2 experiments are shown in Figure 12.

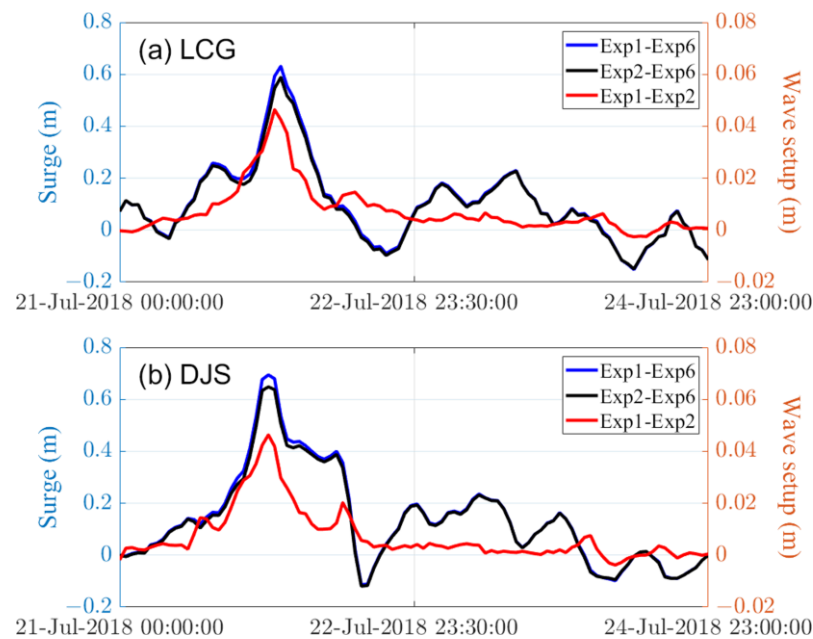


Figure 12. Time series of wave setup and surge from Exp1 and Exp2 at (a) LCG station and (b) DJS station.

At the LCG station, the peak of wave setup reached 0.05 m at 23:00 on 21 July, while the peak of storm surge occurred at 01:00 the following day. At the DJS station, the peak of wave setup was 0.04 m, coinciding with the peak storm surge. The time of the peak wave setup does not necessarily coincide with the peak of the surge, as the surge is influenced not only by wave breaking but also by factors such as tides, wind fields, and topography.

Figure 13a,d,g shows the spatial distribution of the storm surge during Typhoon Ampil in the offshore waters of Changjiang River Estuary. With the typhoon moving, the storm surge gradually increases in the Changjiang River Estuary and its northern regions, reaching a maximum height of up to 2 m. As Typhoon Ampil approaches Shanghai, offshore winds dominate Xiangshan Bay and Sanmen Bay, resulting in water reduction.

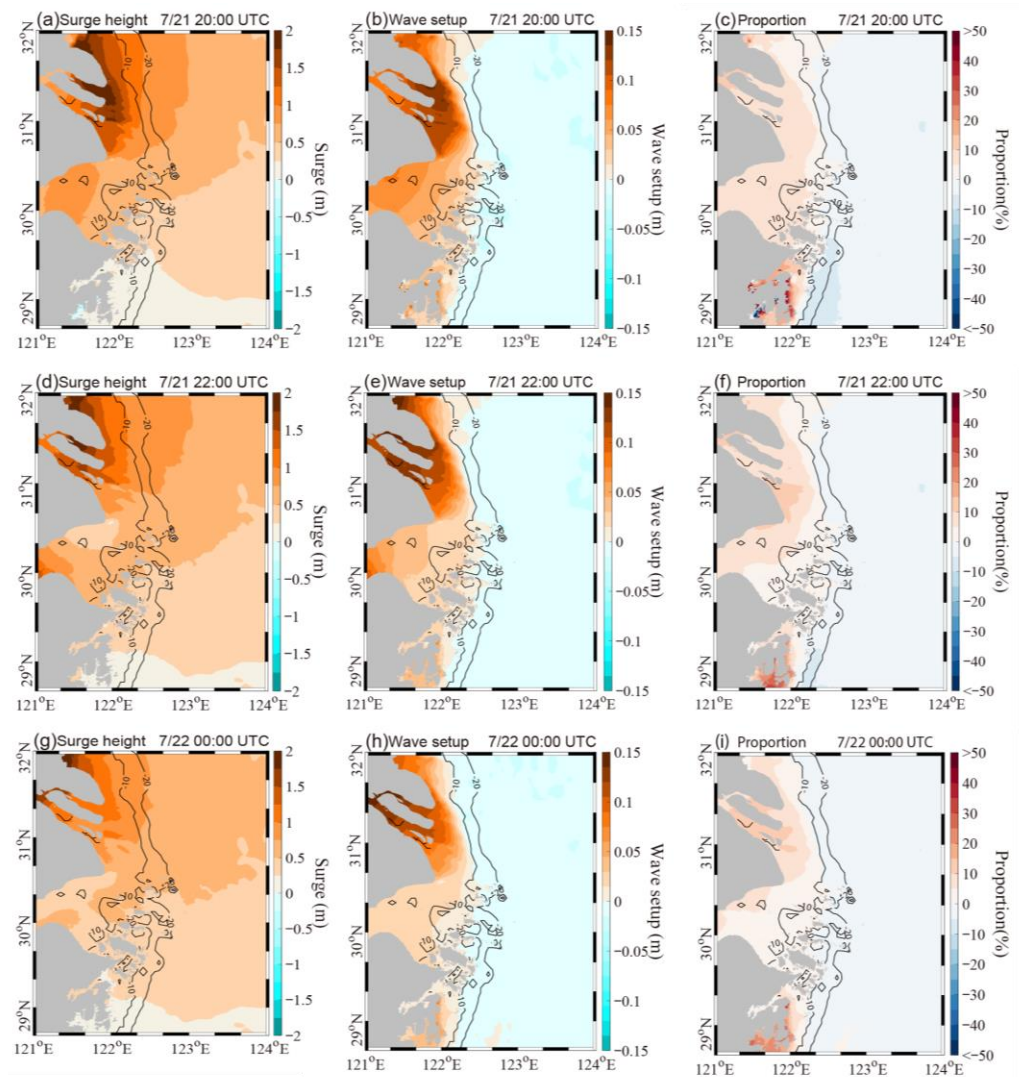


Figure 13. In the offshore area of Changjiang River Estuary, the storm surge (a,d,g), the wave-induced storm surge (b,e,h), and the proportion of the wave-induced storm surge to the storm surge (c,f,i) at 20:00, 22:00 on 21 July, and 0:00 on 22 July.

The maximum wave setup occurs in the Yangtze estuary and peaks at around 0.15 metres (Figure 13b,e,h). Compared to previous major typhoon events, the impact of waves on storm surge during this period is relatively small. Soo Youl Kim conducted a series of experiments to illustrate this phenomenon: during the high tide of astronomical tides, the higher the water levels, the lower the peak of the storm surge caused by wave action [45]. Conversely, at low tide, when the water levels are lower, the peak of the storm surge generated by wave action is greater. When the typhoon was approaching, the Changjiang River Estuary experienced a period of astronomical neap tides with a tidal range of about 2 m. According to Kim’s calculations, the wave-induced storm surge was about 0.1 m. This explains the relatively small peak of the wave-induced surge during Typhoon Ampil.

The spatial distribution of the storm surge caused by wave radiation stress follows a certain pattern: in offshore regions, wave radiation stress causes a decrease in water levels. However, as the waves approach the coastal areas with a water depth of about 10 m or less, the wave radiation stress causes the water levels to rise. The contribution of wave setup to the total storm surge is shown in Figure 13c,f,i, with the largest contribution observed at Xiangshan Bay and Sanmen Bay, where wave setup accounts for more than 30%.

5. Conclusions

In this study, a wave-tide coupling model SCHISM-WWMIII is applied to investigate the wave-tide interactions in the Changjiang River Estuary and its adjacent coastal areas during Typhoon Ampil in July 2018. Both the CFSv2 and the ERA5 datasets were used as the atmospheric forcing conditions of the coupling model for the comparison of the model performances. The model forcing by ERA5 underpredicted the SWH, which exceeded 6.0 m. However, a better performance was obtained by employing the CFSv2 for Typhoon Ampil. The simulation result from the coupling model which utilized the CFSv2 atmosphere fields is reasonable for the study of wave-tide interactions during Typhoon Ampil. The accuracy of the wind field is one of the most important factors in the simulation of wave height, and the physical parameterization schemes of the wave model as well as the corresponding parameter value settings also affect the wave height predictions.

A set of sensitive experiments were conducted to quantify the effects of tide on SWH and wave setup during Typhoon Ampil. Tide-induced variations in water levels are the main cause of periodic changes in nearshore waves. In the study area, where the water depth is about 10 m or less, waves are significantly influenced by tidal effects. However, in the areas with water depths exceeding 10 m, the key factor in determining wave modulation has shifted from water levels to wind during Typhoon Ampil. Considering the effects of water levels and currents in the simulation of wave model would outperform the wave model which only driven by wind fields. The study reveals that wave-tide coupling would improve the accuracy of wave simulations.

Sensitivity experiments have quantified storm surge and wave-induced storm surge. During Typhoon Ampil, wave radiation stress plays a significant role in the storm surge. In coastal areas shallower than 10 m deep, wave radiation stress causes the water levels to rise, reaching a maximum of 0.15 m or more. Wave setup accounted for 10% to 20% of the total surge in the Changjiang River Estuary and Hangzhou Bay, and more than 30% in Xiangshan Bay and Sanmen Bay.

The results of the present study investigate the wave-tide interaction on SWH and quantify the wave setup in Typhoon Ampil. However, the research presented in this paper is not comprehensive. Further assessments will be carried out to evaluate the influence of more different wind fields in order to improve the accuracy of the model in simulating significant wave heights, such as some of the higher-resolution synthetic wind fields. Other physical parameterization schemes of the wave model as well as the corresponding parameter value settings will be tested to optimize the wave simulation in the Changjiang River Estuary and its adjacent coastal areas. In addition, the incorporation of temperature, salinity fields and large-scale estuarine currents will allow for a more comprehensive analysis of wave-tide interactions and their effects on the hydrodynamic environment [78]. These efforts will contribute to improving the accuracy of hindcasting and forecasting in the model. Besides, more typhoons will be simulated to try to draw some general conclusions.

Author Contributions: Conceptualization, Y.Z., M.X., Y.W., Y.T. and Q.J.; methodology, Q.J. and Y.Z.; validation, Q.J., M.X. and Y.Z.; investigation, Q.J., Y.W. and Y.Z.; writing—original draft preparation, Q.J., Y.T. and Y.Z.; writing—review and editing, Q.J. and Y.Z.; visualization, Y.Z.; funding acquisition, Q.J. All authors have read and agreed to the published version of the manuscript.

Funding: This research was funded by the Basic Public Welfare Research Project of Zhejiang Province (grant no. LGF22D060001), the National Natural Science Foundation of China (41806004), the Basic Scientific Research Business Expenses of Zhejiang Provincial Universities (grant no. 2020J00008).

Institutional Review Board Statement: Not applicable.

Informed Consent Statement: Not applicable.

Data Availability Statement: Supporting data can be made available upon request.

Acknowledgments: We would like to appreciate the Chinese Academy of Sciences for the observed wave height data, and also appreciate the National Marine Data and Information Service for tide data.

Conflicts of Interest: The authors declare no conflict of interest.

References

1. Zhou, C.; Yin, C.; Zhang, W.; Xiong, M.; Zhang, J. Numerical simulation on surge due to landfall of typhoon in the Yangtze Estuary: Ampil (No.1810) as an example. *Hydro-Sci. Mar. Eng.* **2021**, *1*, 70–77.
2. Chen, C.; Beardsley, R.C.; Luettich, R.A.; Westerink, J.J.; Wang, H.; Perrie, W.; Xu, Q.; Dohahue, A.S.; Qi, J.; Lin, H.; et al. Extratropical storm inundation testbed: Intermodal comparisons in Scituate, Massachusetts. *J. Geophys. Res. Oceans* **2013**, *118*, 5054–5073. [[CrossRef](#)]
3. Chen, C.; Lin, Z.; Beardsley, R.C.; Shyka, T.A.; Zhang, Y.; Xu, Q.; Qi, J.; Lin, H.; Xu, D. Impacts of sea level rise on future storm-induced coastal inundations over massachusetts coast. *Nat. Hazards* **2021**, *106*, 375–399. [[CrossRef](#)]
4. Liu, Z.; Wang, H.; Zhang, Y.J.; Magnusson, L.; Loftis, J.D.; Forrest, D. Cross-scale modeling of storm surge, tide, and inundation in Mid-Atlantic Bight and New York City during Hurricane Sandy, 2012. *Estuar. Coast. Shelf Sci.* **2020**, *233*, 106544. [[CrossRef](#)]
5. Chi, Y.; Rong, Z. Assessment of Extreme Storm Surges over the Changjiang River Estuary from a Wave–Current Coupled Model. *J. Mar. Sci. Eng.* **2021**, *9*, 1222. [[CrossRef](#)]
6. Irish, J.L.; Resio, D.T. A hydrodynamics-based surge scale for hurricanes. *Ocean Eng.* **2010**, *37*, 69–81. [[CrossRef](#)]
7. Salmun, H.; Molod, A. The Use of a Statistical Model of Storm Surge as a Bias Correction for Dynamical Surge Models and its Applicability along the U.S. East Coast. *J. Mar. Sci. Eng.* **2015**, *3*, 73–86. [[CrossRef](#)]
8. Araki, Y.; Tomohiro, Y.; Adrean, W.; Nobuhito, M. Statistical prediction of storm surge height time series by convolutional neural network and its long-term projection. *J. Jpn. Soc. Civ. Eng.* **2020**, *76*, 1093–1098. [[CrossRef](#)]
9. Islam, M.R.; Lee, C.Y.; Mandli, K.T.; Takagi, H. A new tropical cyclone surge index incorporating the effects of coastal geometry, bathymetry and storm information. *Sci. Rep.* **2021**, *11*, 16747. [[CrossRef](#)]
10. Bretschneider, C.L. Hurricane design—Wave practices. *J. Waterw. Harb. Div.* **1957**, *124*, 39–62. [[CrossRef](#)]
11. Neumann, G.; Pierson, W.J. A detailed comparison of theoretical wave spectra and wave forecasting methods. *Dtsch. Hydrogr. Zeitschrift.* **1957**, *10*, 73–92. [[CrossRef](#)]
12. Luettich, R.A.; Westerink, J.J. *Formulation and Numerical Implementation of the 2D/3D ADCIRC Finite Element Model Version 44.XX*; University of North Carolina at Chapel Hill: Morehead City, NC, USA, 2004.
13. Ding, Y.; Yao, Z.G.; Zhou, L.L.; Bao, M.; Zang, Z.C. Numerical modeling of the seasonal circulation in the coastal ocean of the Northern South China Sea. *Front. Earth Sci.* **2018**, *14*, 90–109. [[CrossRef](#)]
14. Lesser, G.R.; Roelvink, J.A.; van Kester, J.A.T.M.; Stelling, G.S. Development and validation of a three-dimensional morphological model. *Coast. Eng.* **2004**, *51*, 883–915. [[CrossRef](#)]
15. Warren, I.R.; Bach, H.K. MIKE 21: A modelling system for estuaries, coastal waters and seas. *Environ. Model. Softw.* **1992**, *7*, 229–240. [[CrossRef](#)]
16. Shchepetkin, A.F.; McWilliams, J.C. The regional oceanic modeling system (ROMS): A split-explicit, free-surface, topography-following-coordinate oceanic model. *Ocean Model.* **2005**, *9*, 347–404. [[CrossRef](#)]
17. Palma, E.D.; Matano, R.P. On the implementation of passive open boundary conditions for a general circulation model: The barotropic mode. *J. Geophys. Res. Oceans* **1998**, *103*, 1319–1341. [[CrossRef](#)]
18. Hansen, J.E.; Elias, E.; List, J.H.; Erikson, L.H.; Barnard, P.L. Tidally influenced alongshore circulation at an inlet-adjacent shoreline. *Cont. Shelf Res.* **2013**, *56*, 26–38. [[CrossRef](#)]
19. Moon, I.J.; Kwon, J.I.; Lee, J.C.; Shim, J.; Kang, S.K.; Oh, I.S.; Kwon, S.J. Effect of the surface wind stress parameterization on the storm surge modeling. *Ocean Model.* **2009**, *29*, 115–127. [[CrossRef](#)]
20. Blain, C.A.; Westerink, J.J. The influence of domain size on the response characteristics of a hurricane storm surge model. *J. Geophys. Res.* **1994**, *99*, 18467–18479. [[CrossRef](#)]
21. Shen, J.; Gong, W.; Wang, H.V. Water level response to 1999 Hurricane Floyd in the Chesapeake Bay. *Cont. Shelf Res.* **2006**, *26*, 2484–2502. [[CrossRef](#)]
22. Irish, J.L.; Resio, D.T.; Ratcliff, J.J. The Influence of Storm Size on Hurricane Surge. *J. Phys. Oceanogr.* **2006**, *38*, 2003–2013. [[CrossRef](#)]
23. Zhong, L.; Li, M.; Zhang, D.L. How do uncertainties in hurricane model forecasts affect storm surge predictions in a semi-enclosed bay? *Estuar. Coast. Shelf Sci.* **2010**, *90*, 61–72. [[CrossRef](#)]
24. Ringler, T.; Petersen, M.; Higdon, R.L.; Jacobsen, D.; Jones, P.W.; Maltrud, M. A multi-resolution approach to global ocean modeling. *Ocean Model.* **2013**, *69*, 211–232. [[CrossRef](#)]
25. Li, A.; Guan, S.; Mo, D.; Hou, Y.; Hong, X.; Liu, Z. Modeling wave effects on storm surge from different typhoon intensities and sizes in the South China Sea. *Estuar. Coast. Shelf Sci.* **2020**, *235*, 106551. [[CrossRef](#)]
26. Yin, K.; Xu, S.; Huang, W.; Xie, Y. Effects of sea level rise and typhoon intensity on storm surge and waves in Pearl River Estuary. *Ocean Eng.* **2017**, *136*, 80–93. [[CrossRef](#)]
27. Feng, X.; Yin, B.; Yang, D. Effect of hurricane paths on storm surge response at Tianjin, China. *Estuar. Coast. Shelf Sci.* **2012**, *106*, 58–68. [[CrossRef](#)]
28. Islam, M.R.; Takagi, H. Typhoon parameter sensitivity of storm surge in the semi-enclosed Tokyo Bay. *Front. Earth Sci.* **2020**, *14*, 553–567. [[CrossRef](#)]

29. Booij, N.; Ris, R.C.; Holthuijsen, L.H. A third-generation wave model for coastal regions: 1. Model description and validation. *J. Phys. Oceanogr.* **1999**, *104*, 7649–7666. [[CrossRef](#)]
30. Tolman, H.L. *WAVEWATCH III Development Group. User Manual and System Documentation of WAVEWATCH III*; National Oceanic and Atmospheric Administration (NOAA): Washington, DC, USA, 2014.
31. Zijlema, M.; Vledder, G.P.; Holthuijsen, L.H. Bottom friction and wind drag for wave models. *Coast. Eng.* **2012**, *65*, 19–26. [[CrossRef](#)]
32. Chen, H.S. Effects of bottom friction and boundary absorption on water wave scattering. *Appl. Ocean Res.* **1986**, *8*, 99–104. [[CrossRef](#)]
33. Lee, J.W.; Irish, J.L.; Michelle, T.B.; Marcy, D.C. Rapid prediction of peak storm surge from tropical cyclone track time series using machine learning. *Coast. Eng.* **2021**, *170*, 104024. [[CrossRef](#)]
34. Valle, R.; Alexandra, N.; Curchitser, E.N.; Bruyère, C.L.; McOwen, S. Implementation of an Artificial Neural Network for Storm Surge Forecasting. *J. Geophys. Res.* **2021**, *126*, e2020JD033266. [[CrossRef](#)]
35. Park, Y.; Kim, E.; Choi, Y.; Seo, G.; Kim, Y.; Kim, H. Storm Surge Forecasting along Korea Strait Using Artificial Neural Network. *J. Mar. Sci. Eng.* **2022**, *10*, 535. [[CrossRef](#)]
36. Ali, M.; Ramendra, P. Significant wave height forecasting via an extreme learning machine model integrated with improved complete ensemble empirical mode decomposition. *Renew. Sustain. Energy Rev.* **2019**, *104*, 281–295. [[CrossRef](#)]
37. Shahaboddin, S.; Mosavi, A.H.; Rabczuk, T.; Nabipour, N.; Chau, K. Prediction of significant wave height; comparison between nested grid numerical model, and machine learning models of artificial neural networks, extreme learning and support vector machines. *Eng. Appl. Comput. Fluid Mech.* **2020**, *14*, 805–817.
38. Demetris, D.; Michailides, C.; Papanastasiou, G.; Onoufriou, T. Coastal zone significant wave height prediction by supervised machine learning classification algorithms. *Ocean Eng.* **2021**, *221*, 108592. [[CrossRef](#)]
39. Wolf, J.; Prandle, D. Some observations of wave–current interaction. *Coast. Eng.* **1999**, *37*, 471–485. [[CrossRef](#)]
40. Olabarrieta, M.; Geyer, R.W.; Kumar, N. The role of morphology and wave-current interaction at tidal inlets: An idealized modeling analysis. *J. Geophys. Res. Oceans* **2014**, *119*, 8818–8837. [[CrossRef](#)]
41. Elahi, M.W.E.; Wang, X.H.; Salcedo-Castro, J.; Ritchie, E.A. Influence of Wave–Current Interaction on a Cyclone-Induced Storm Surge Event in the Ganges–Brahmaputra–Meghna Delta: Part 1—Effects on Water Level. *J. Mar. Sci. Eng.* **2023**, *11*, 328. [[CrossRef](#)]
42. Olabarrieta, M.; Warner, J.C.; Kumar, N. Wave-current interaction in Willapa Bay. *J. Geophys. Res.* **2011**, *116*, C12014. [[CrossRef](#)]
43. Jonsson, I.G.; Skougaard, C.; Wang, J.D. Interaction between waves and currents. *Coast. Eng.* **1970**, *1*, 489–507. [[CrossRef](#)]
44. Jonsson, I.G. Measurements in the turbulent wave boundary layer. *Int. Ass. Hydr. Res. 10th Congr.* **1963**, *1*, 85–92.
45. Kang, K.R.; Kim, S. Wave–tide interactions during a strong storm event in Kyunggi Bay, Korea. *Ocean Eng.* **2015**, *108*, 10–20. [[CrossRef](#)]
46. Lewis, M.J.; Palmer, T.; Hashemi, R.; Robins, P.E.; Saulter, A.; Brown, J.M.; Lewis, H.W.; Neill, S.P. Wave-tide interaction modulates nearshore wave height. *Ocean Dyn.* **2019**, *69*, 367–384. [[CrossRef](#)]
47. Idier, D.; Bertin, X.; Thompson, P.; Pickering, M.D. Interactions Between Mean Sea Level, Tide, Surge, Waves and Flooding: Mechanisms and Contributions to Sea Level Variations at the Coast. *Surv. Geophys.* **2019**, *40*, 1603–1630. [[CrossRef](#)]
48. Longuet-Higgins, M.S.; Stewart, R. Radiation stress and mass transport in gravity waves, with application to ‘surf beats’. *J. Fluid Mech.* **1962**, *13*, 481–504. [[CrossRef](#)]
49. Longuet-Higgins, M.S.; Stewart, R. Radiation stresses in water waves; a physical discussion, with applications. *Deep-Sea Res* **1964**, *11*, 529–562. [[CrossRef](#)]
50. Xie, L.; Liu, H.; Peng, M. The effect of wave–current interactions on the storm surge and inundation in Charleston Harbor during Hurricane Hugo 1989. *Ocean Model.* **2008**, *20*, 252–269. [[CrossRef](#)]
51. Sebastian, A.; Proft, J.; Casey Dietrich, J.; Du, W.; Bedient, P.B.; Dawson, C.N. Characterizing hurricane storm surge behavior in Galveston Bay using the SWAN+ADCIRC model. *Coast. Eng.* **2014**, *88*, 171–181. [[CrossRef](#)]
52. Vijayan, L.; Huang, W.; Ma, M.; Ozguven, E.; Ghorbanzadeh, M.; Yang, J.; Yang, Z. Improving the accuracy of hurricane wave modeling in Gulf of Mexico with dynamically-coupled SWAN and ADCIRC. *Ocean Eng.* **2023**, *274*, 114044. [[CrossRef](#)]
53. Hong, J.-S.; Moon, J.-H.; Kim, T. Effect of Breaking Waves on Near-Surface Mixing in an Ocean-Wave Coupling System under Calm Wind Conditions. *J. Mar. Sci. Eng.* **2020**, *8*, 540–555. [[CrossRef](#)]
54. Benetazzo, A.; Carniel, S.; Sclavo, M.; Bergamasco, A. Wave–current interaction: Effect on the wave field in a semi-enclosed basin. *Ocean Model.* **2013**, *70*, 152–165. [[CrossRef](#)]
55. Liu, C.; Jia, Y.; Onat, Y.; Cifuentes-Lorenzen, A.; Ilija, A.; McCardell, G.; Fake, T.; O’Donnell, J. Estimating the Annual Exceedance Probability of Water Levels and Wave Heights from High Resolution Coupled Wave-Circulation Models in Long Island Sound. *J. Mar. Sci. Eng.* **2020**, *8*, 475–495. [[CrossRef](#)]
56. Qi, J.; Chen, C.; Beardsley, R.C.; Perrie, W.; Cowles, G.W.; Lai, Z. An unstructured-grid finite-volume surface wave model (FVCOM-SWAVE): Implementation, validations and applications. *Ocean Model.* **2009**, *28*, 153–166. [[CrossRef](#)]
57. Lavaud, L.; Bertin, X.; Martins, K.; Arnaud, G.; Bouin, M.-N. The contribution of short-wave breaking to storm surges: The case Klaus in the Southern Bay of Biscay. *Ocean Model.* **2020**, *156*, 101710. [[CrossRef](#)]
58. Daniels, T.; Fearon, G.; Vilaplana, A.; Hewitson, B.; Rautenbach, C. On the importance of wind generated waves in embayments with complex orographic features—A South African case study. *Appl. Ocean Res.* **2022**, *128*, 103355. [[CrossRef](#)]

59. Kim, S.Y.; Yasuda, T.; Mase, H. Numerical analysis of effects of tidal variations on storm surges and waves. *Appl. Ocean Res.* **2008**, *30*, 311–322. [[CrossRef](#)]
60. Mengual, B.; Bertin, X.; Place, F.; Pezerat, M.; Coulombier, T.; Mendes, D.; Fortunato, A.B. Wave-current interactions at the Tagus Estuary Mouth (Portugal) under storm wave conditions. *Ocean Model.* **2022**, *175*, 102035. [[CrossRef](#)]
61. Du, M.; Hou, Y.; Qi, P.; Wang, K. The impact of different historical typhoon tracks on storm surge: A case study of Zhejiang, China. *J. Mar. Sci.* **2020**, *206*, 103318. [[CrossRef](#)]
62. He, Z.; Tang, Y.; Xia, Y.; Chen, B.; Xu, J.; Yu, Z.; Li, L. Interaction impacts of tides, waves and winds on storm surge in a channel-island system: Observational and numerical study in Yangshan Harbor. *Ocean Dyn.* **2020**, *70*, 307–325. [[CrossRef](#)]
63. Hsiao, S.-C.; Chen, H.; Chen, W.-B.; Chang, C.-H.; Lin, L.-Y. Quantifying the contribution of nonlinear interactions to storm tide simulations during a super typhoon event. *Ocean Eng.* **2019**, *194*, 106661. [[CrossRef](#)]
64. Song, H.; Kuang, C.; Wang, X.H.; Ma, Z. Wave-current interactions during extreme weather conditions in southwest of Bohai Bay, China. *Ocean Eng.* **2020**, *216*, 108068. [[CrossRef](#)]
65. Zhang, Y.J.; Ye, F.; Stanev, E.V.; Grashorn, S. Seamless cross-scale modeling with SCHISM. *Ocean Model.* **2016**, *102*, 64–81. [[CrossRef](#)]
66. Zhang, Y.; Baptista, A. SELFE: A semi-implicit Eulerian-Lagrangian finite-element model for cross-scale ocean circulation. *Ocean Model.* **2008**, *21*, 71–96. [[CrossRef](#)]
67. Roland, A. Development of WWMI II: Spectral Wave Modeling on Unstructured Meshes. Ph.D. Thesis, The Institute of Hydraulic and Water Resources Engineering, Darmstadt University of Technology, Darmstadt, Germany, 2008.
68. Roland, A.; Zhang, Y.; Wang, H.V.; Meng, Y.; Teng, Y.; Maderich, V.; Brovchenko, I.; Dutour-Sikiric, M.; Zanke, U. A fully coupled wave-current model on unstructured grids. *J. Geophys. Res.* **2012**, *117*, C00J33. [[CrossRef](#)]
69. Hsu, T.-W.; Ou, S.-H.; Liau, J.-M. Hindcasting nearshore wind waves using a FEM code for SWAN. *Coast. Eng.* **2005**, *52*, 177–195. [[CrossRef](#)]
70. Wessel, P.; Smith, W.H.F. A Global Self-consistent, Hierarchical, High-resolution Shoreline Database. *J. Geophys. Res.* **1996**, *101*, 8741–8743. [[CrossRef](#)]
71. Mayer, L.; Jakobsson, M.; Allen, G.; Dorschel, B.; Falconer, R.; Ferrini, V.; Lamarche, G.; Snaith, H.; Weatherall, P. The Nippon Foundation—GEMCO Seabed 2030 Project: The Quest to See the World’s Oceans Completely Mapped by 2030. *Geosci. J.* **2018**, *8*, 63. [[CrossRef](#)]
72. Lyard, F.H.; Allain, D.J.; Cancet, M.; Carrère, L.; Picot, N. FES2014 Global ocean tide atlas: Design and performance. *Ocean Sci.* **2021**, *17*, 615–649. [[CrossRef](#)]
73. Saha, S.; Moorthi, S.; Wu, X.; Wang, J.; Nadiga, S.; Tripp, P.; Behringer, D.; Hou, Y.; Chuang, H.; Iredell, M.; et al. The NCEP Climate Forecast System Version 2. *J. Clim.* **2014**, *27*, 2185–2208. [[CrossRef](#)]
74. Hersbach, H.; Bell, B.; Berrisford, P.; Biavati, G.; Horányi, A.; Muñoz Sabater, J.; Nicolas, J.; Peubey, C.; Radu, R.; Rozum, I.; et al. ERA5 hourly data on single levels from 1940 to present. *Copernic. Clim. Change Serv. Clim. Data Store* **2023**, *146*, 1999–2049. [[CrossRef](#)]
75. Battjes, J.A.; Janssen, J. Energy loss and set-up due to breaking of random waves. In Proceedings of the 16th Conference on Coastal Engineering, Hamburg, Germany, 27 August–3 September 1978; Available online: <http://resolver.tudelft.nl/uuid:2fba43fe-f8bd-42ac-85ee-848312d2e27e> (accessed on 1 January 1978).
76. Hasselmann, K.; Barnett, T.P.; Bouws, E.; Carlson, H.; Cartwright, D.E.; Enke, K.; Ewing, J.A.; Gienapp, H.; Hasselmann, D.E.; Kruseman, P.; et al. *Measurements of Wind-Wave Growth and Swell Decay during the Joint North Sea Wave Project (JONSWAP)*; Deutsches Hydrographisches Institut: Hamburg, Germany, 1973; Available online: <http://resolver.tudelft.nl/uuid:f204e188-13b9-49d8-a6dc-4fb7c20562fc> (accessed on 1 January 1973).
77. Wang, C.; Wang, X.; Liu, C.; Jia, S.; Wang, Y. A Typhoon Dataset of the Yellow Sea and East China Sea from 2010 to 2018. *Sci. Data Bank* **2020**, *5*. [[CrossRef](#)]
78. Bennis, A.-C.; Furgerot, L.; Bailly Du Bois, P.; Poizot, E.; Méar, Y.; Dumas, F. A winter storm in Alderney Race: Impacts of 3D wave–current interactions on the hydrodynamic and tidal stream energy. *Appl. Ocean Res.* **2022**, *120*, 103009. [[CrossRef](#)]

Disclaimer/Publisher’s Note: The statements, opinions and data contained in all publications are solely those of the individual author(s) and contributor(s) and not of MDPI and/or the editor(s). MDPI and/or the editor(s) disclaim responsibility for any injury to people or property resulting from any ideas, methods, instructions or products referred to in the content.